Tailored Charge Transfer Kinetics in Precursors for Organic Radical Batteries: A Joint Synthetic-Theoretical Approach**

Clara Zens,[a] Christian Friebe,[b, c] Ulrich S. Schubert,[b, c] Martin Richter,[a, d] and Stephan Kupfer*[a]

The development of sustainable energy storage devices is crucial for the transformation of our energy management. In this scope, organic batteries attracted considerable attention. To overcome the shortcomings of typically applied materials from the classes of redox-active conjugated polymers (i.e., unstable cell voltages) and soft matter-embedded stable organic radicals (i.e., low conductivity), a novel design concept was introduced, integrating such stable radicals within a conductive polymer backbone. In the present theory-driven design approach, redox-active (2,2,6,6-tetramethylpiperidin-1-yl)oxyls (TEMPOs) were incorporated in thiophene-based polymer model systems, while structure-property relationships governing the thermodynamic properties as well as the charge transfer kinetics underlying the charging and discharging processes were investigated in a systematical approach. Thereby, the impact of the substitution pattern, the length as well as the nature of the chemical linker, and the ratio of TEMPO and thiophene units was studied using state-of-the-art quantum chemical and quantum dynamical simulations for a set of six molecular model systems. Finally, two promising candidates were synthesized and electrochemically characterized, paving the way to applications in the frame of novel organic radical batteries.

Introduction

Nowadays, small, lightweight, mechanically flexible and stable, safe, as well as inexpensive energy storage solutions are desired due to the rising impact of mobile devices, smart packaging and clothing, and the Internet of Things. Current mobile energy storage is mainly based on lithium-ion batteries, which exhibit several disadvantages. In particular, the possibility of fire or even explosions in case of leakage or breaking of the battery constitutes a major risk through the application of lithium-based energy storage.[1,2] Furthermore, such batteries depend on the, usually ecologically harmful, exploitation of critical resources, like nickel, manganese, and cobalt,[3] as well as on

their disposal or recycling.[4,5] Thus, to enable a future sustainable electrochemical energy storage, alternative technologies have to be explored.[6,7] Organic batteries, replacing metals or metal oxides with organic or polymeric active materials, represent a promising approach, which does not rely on controversial resource deposits. Instead, the active materials can be potentially synthesized from renewable sources in the future.[8] Additionally, organic, polymeric materials allow for a more comprehensive processability, enabling the application of different casting methods like printing (e.g., screen printing, inkjet printing), doctor blading, or roll-to-roll manufacturing, leading, furthermore, to the production of mechanically flexible devices.[9]

Among the possible candidates, conjugated polymers were the first to be used as active materials in organic electrochemical energy storage.[10,11] However, conjugated polymers possess a semiconductor-like electronic band structure, which is formed by the overlap of the π-orbitals of the single repetition units of the polymer.[12,13] Consequently, their redox potentials depend strongly on the state of charge,[14] and the utilized systems are incapable of providing stable discharge voltages and capacities, which led to a prompt abandonment of this approach. Nevertheless, the described band structure provides an increased electronic and ionic conductivity, when the polymer is partially oxidized or reduced, leading to a decreased need for conductive additives. Furthermore, conjugated polymers can be potentially formed via electrochemical polymerization, which enables in situ formation of electrode films.[15,16]

Recently, stable organic radicals are among the most popular compound classes for active materials in organic batteries. They are characterized by an unpaired electron that is stabilized through sterically demanding substituents or electron resonance. In contrast to other types of redox-active materials,

[a] C. Zens, Dr. M. Richter, Dr. S. Kupfer
Institute of Physical Chemistry, Friedrich Schiller University Jena
Helmholtzweg 4, 07743 Jena (Germany)
E-mail: stephan.kupfer@uni-jena.de
[b] Dr. C. Friebe, Prof. Dr. U. S. Schubert
Laboratory of Organic and Macromolecular Chemistry (IOMC)
Friedrich Schiller University Jena
Humboldtstraße 10, 07743 Jena (Germany)
[c] Dr. C. Friebe, Prof. Dr. U. S. Schubert
Center for Energy and Environmental Chemistry Jena (CEEC Jena)
Friedrich Schiller University Jena
Philosophenweg 7a, 07743 Jena (Germany)
[d] Dr. M. Richter
DS Deutschland GmbH
Am Kabellager 11–13, 51063 Cologne (Germany)

ChemSusChem

Research Article
doi.org/10.1002/cssc.202201679

**Chemistry
Europe**
European Chemical
Societies Publishing

their charged state is a non-radical, and thus more stable, one. Furthermore, the addressed redox processes involve only the transfer of a single electron without larger structural changes, which leads to fast redox kinetics; thus, high charging and discharging currents and high power densities are possible.[17]

Within this contribution, we pursue a novel design approach by combining conjugated polymers and stable organic radicals in the scope of p-type electrode materials. Thereby, the conjugated polymer forms the backbone of the material in order to provide a good conductivity during charging and discharging, while the stable organic radicals attached to the conductive backbone facilitate a constant voltage over a broad range of capacities. During the charging process, the positive charge is initially transferred via the backbone and subsequently towards the organic radical. Energy storage within the charged cathode (half-)cell is rationalized by oxidation of the radical moieties and by localizing the positive charges (or holes) on the redox-active units. When the half-cell is discharged, the charge is transferred back from the radical to the backbone, where the charge is conducted towards the current collector.

On a molecular level, such p-type electrode material should exhibit mainly four characteristics: (i) The backbone should have a good conductivity. (ii) The potential coupling of the charge transfer from the stable organic radical to the conducting backbone needs to be reasonably high to allow an electronic interaction between the involved donor and acceptor states. Only then, an efficient charge transfer is possible. Hence, the potential coupling ($H_{\delta\alpha}^{\mathrm{dia}}$) constitutes the key parameter for fast charging and discharging processes. (iii) Charge localization within the charged polymer is provided by the redox-active, yet stable, radical moieties. Thus, the Gibbs energy or driving force (ΔG) of the charge transfer from the radical to the backbone needs to be positive. Otherwise, the charge will be partially delocalized on the backbone leading to instable capacities of the half-cell.[18] (iv) The activation energy of the charge transfer should be small.

On the quest for this holy grail of a redox-active polymer, we investigated several model systems. Initially, we focused our theory-driven design approach on thiophene-based polymers, which feature highly promising properties with respect to conductivity as well as thermal and (electro)chemical stability.[19,20] In the frame of stable organic radicals, the well-known and thoughtfully investigated (2,2,6,6-tetramethylpiperidin-1-yl)oxyl (TEMPO) as well as its derivatives are the redox-active units of choice. Moreover, several polymers functionalized with TEMPO were already successfully implemented as cathode material in batteries.[21–24] This new family of redox-active materials resulting from the combination of a thiophene-based polymer with TEMPO radical units will be investigated in-depth in the present study. Structure-property relationships governing, for example, the redox processes and the underlying charge transfer kinetics are elucidated in a joint synthetic-theoretical approach (see Figure 1a). To this aim, a set of molecular model systems is investigated by quantum chemical and quantum dynamical methods. In literature, several theoretical as well as joint theoretical-experimental studies can
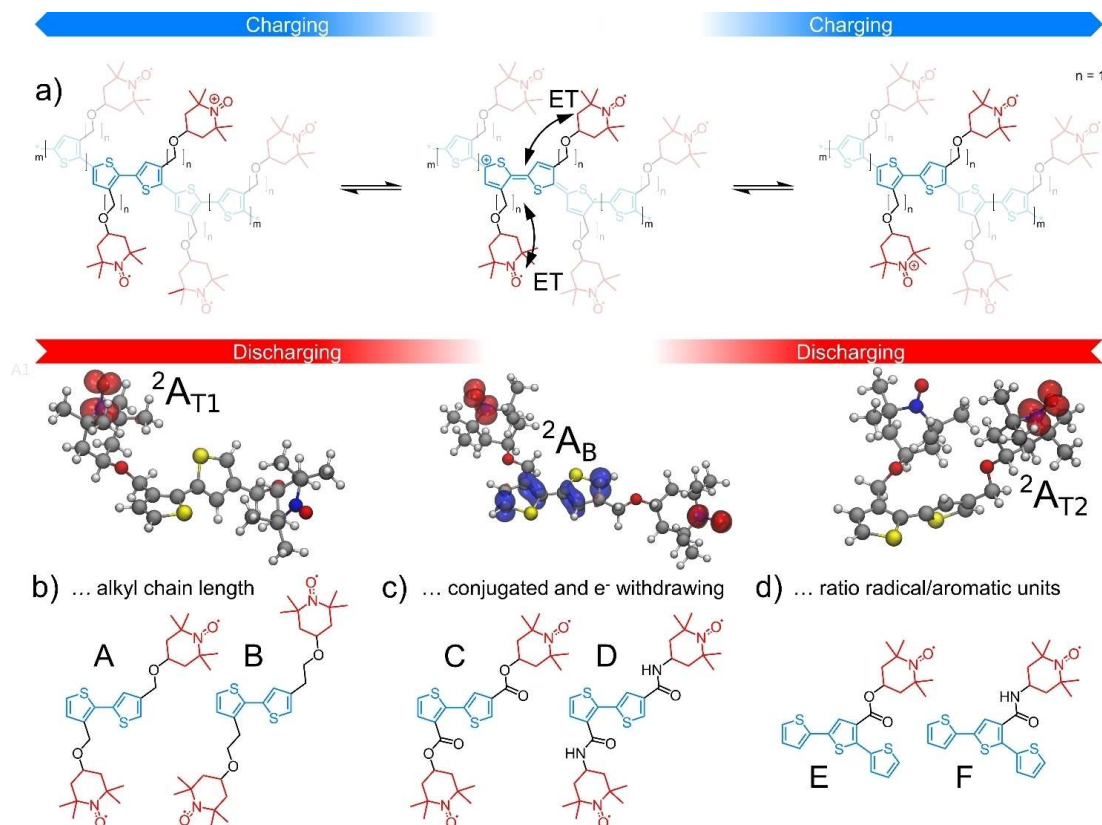
be found that focus on the comparison of calculated charge transfer rate constants obtained using semi-classical Marcus theory and molecular dynamical (MD) simulations. These studies were predominantly performed in the frame of redox cascades in biology and in solar energy conversion.[25–35]

In the current contribution, we follow our recently introduced protocol to assess the thermodynamics and kinetics of intramolecular charge transfer processes along efficient reaction coordinates within the Marcus picture[36–39] as well by means of dissipative quantum dynamics.[40,41]

The molecular model systems are built in a modular approach and consist of an oligo-thiophene decorated by one or two TEMPO units as well as a linker connecting the backbone and the redox-active centers chemically. The applied alkyl vs. conjugated linkers allow the tailoring of the electronic communication among these building blocks (see Figure 1b–d). Thereby, our initial model system, acting as reference for further systems, contains two thiophenes and two TEMPOs connected by an ether (CO) linker. In order to map a larger conformational space, one TEMPO was attached to the outer C-atom of the thiophene (**T1**) and the other TEMPO to the inner C-atom of the thiophene (**T2**) as shown in Figure 1b. Additionally, the bridging linker was varied systematically to assess its influence on the potential coupling as well as on the thermodynamic properties of the charge transfer processes underlying charging and discharging. The reference system, **A**, utilizes an ether CO linker, while the length of the ether's C-chain was enlarged to yield a C_2O linker (**B**, Figure 1b). Further, not only the length but also the chemical nature of the linker was modified. To this aim, an ester-linker (**C**) as well as an amide-linker (**D**) were introduced. Finally, the ratio of the redox units was adjusted to a terthiophene backbone to which merely one TEMPO was attached. These six molecules served as model systems to study the structure-property relationships governing the cell voltage as well as the charging/discharging kinetics of this new class of organic radical batteries, while initial synthetic and electrochemical studies were performed based on the preceding computational investigations.

Results and Discussion

Hole transfer processes between the redox-active units of our model system, namely among the TEMPOs and the thiophene backbone, were investigated. In order to differentiate between the redox intermediates, the notation $^{M}X_C$ is introduced, where the multiplicity of the species is labeled by **M** for the given molecular model system **X**. **C** denotes the position of the positive charge, namely at the outer TEMPO (**T1**), the inner TEMPO (**T2**), or at the thiophene backbone (**B**). Thereby, the potential energy surfaces (PESs) associated to the charge transfer were assessed at the cost-efficient density and time-dependent density functional levels of theory [(TD-)DFT]. Figure 2a illustrates the PESs of **A**, predicted by the range-separated ωB97XD[42] XC functional along linear-interpolated internal coordinates (LIICs) as obtained by pysisyphus[43] (see

ChemSusChem

Research Article
doi.org/10.1002/cssc.202201679

**Chemistry
Europe**
European Chemical
Societies Publishing

Figure 1. (a) Redox species involved in the charging and discharging of the p-type electrode material given by the present system comprising a thiophene-based backbone (in blue), TEMPO moieties (in red), and a linker (in black) connecting the redox-active units. Spin densities illustrate the localization of the radical within the respective redox state exemplarily for **A**. (b–d) Molecular model systems **A**–**F** investigated in their singly oxidized doublet ground states. The molecules differ in their type of linker, **A**–**D**, and their redox unit ratio, **E** and **F**.

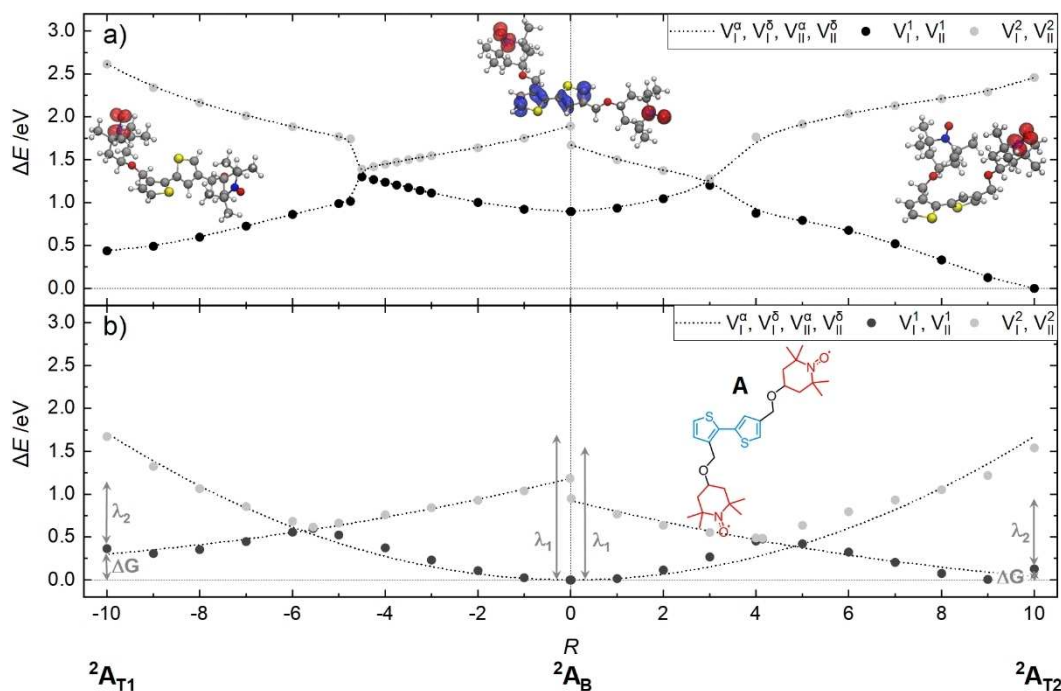Computational methods in the Experimental Section for details).

For **A**, these LIICs mainly involve the planarization of the thiophene backbone as well as a slight rotation of the TEMPO around the carbon atom of the linking moiety. The triradical ground state $^2\mathbf{A_B}$ species is predicted 0.46 eV higher in energy than the $^2\mathbf{A_{T1}}$ species or 0.90 eV higher in energy than the $^2\mathbf{A_{T2}}$ species (see Figure 2a). Therefore, DFT predicts the oxidation of **T1** or **T2** to be thermodynamically more favorable than the oxidation of the bithiophene. Reorganization energies are 1.72 and 1.45 eV for the charge transfer between $^2\mathbf{A_B}$ and $^2\mathbf{A_{T1}}$ as well as 1.57 and 1.67 eV for the charge transfer between $^2\mathbf{A_B}$ and $^2\mathbf{A_{T2}}$.

However, smooth PESs could not be obtained at the (TD-)DFT level of theory. This is particularly evident in the region of the conical intersection. This discontinuity is presumably caused by the single configurational character of DFT. Therefore, DFT is incapable to describe the degeneracy of the mono- and triradical at the conical intersection as well as the degeneracy of the doublet and quartet states within the triradical species. Consequently, DFT does not allow an unambiguous prediction of the PESs and underlying thermodynamic properties for the redox processes of interest within the present organic radical battery (ORB) model system.

To overcome this obstacle, multiconfigurational simulations were performed by means of CASSCF (complete active space self-consistent field)[44,45] along the same reaction coordinates. The applied active space (15,13) comprised the frontier orbitals of the aromatic backbone as well as of both TEMPOs (see Computational details, Figure 7). This time, smooth PESs were obtained. Thus, the thermodynamic properties, such as the driving force ΔG and the reorganization energy λ, and the electronic coupling $H_{\delta\alpha}^{\text{dia}}$ can be estimated. For further information the reader is referred to the Computational details. Table 1 summarizes these values for **A** and for all further investigated ORB model systems, **B**–**F**.

In comparison to the previously discussed (TD-)DFT results, the reorganization energies are hardly affected by the extension of the computational level to multiconfigurational simulations. However, the sign of the system's driving force is reversed as CASSCF energetically favors the oxidation of the bithiophene (triradical intermediate) over TEMPO oxidation (monoradical) by 0.13 to 0.36 eV.

The electronic couplings obtained with the minimum energy splitting method [Eq. (4) in Computational details] are depending on the TEMPO involved in the charge transfer. The coupling for the $^2\mathbf{A_{T1}} \rightleftarrows {}^2\mathbf{A_B}$ charge transfer amounts to 0.0075 eV, while the coupling of the charge transfer of $^2\mathbf{A_{T2}} \rightleftarrows {}^2\mathbf{A_B}$

ChemSusChem

Research Article
doi.org/10.1002/cssc.202201679

Chemistry
Europe
European Chemical
Societies Publishing

Figure 2. (a) Adiabatic PESs of the doublet ground state (in black) as well as of the first excited doublet state of **A** obtained by TD-DFT with respective TEMPO and thiophene backbone being involved (in gray). Efficient hole transfer reaction coordinates are described by linear-interpolated internal coordinates connecting the fully equilibrated redox intermediates $^2A_{T1}$, ^2A_B and $^2A_{T2}$; their electronic nature is visualized by spin densities. (b) PESs of the hole transfer processes (**A**) calculated by CASSCF. Dots represent energies of adiabatic states, corresponding potential energies V are labeled with Arabic numbers. Dotted lines represent respective diabatic surfaces, corresponding potential energies V are labeled with α for the acceptor state and δ for the donor state. Latin numbers denote the charge transfer reactions $^2A_{T1} \rightleftarrows ^2A_B$ (I) or $^2A_{T2} \rightleftarrows ^2A_B$ (II).

Table 1. Electronic coupling $H_{\delta\alpha}^{dia}$, driving force ΔG (given for discharging, $^M X_T \rightarrow ^M X_B$) and reorganization energy λ obtained at the CASSCF level of theory. Electronic couplings are calculated with the minimum energy splitting method and by the fragment charge difference (FCD) method (in parentheses).

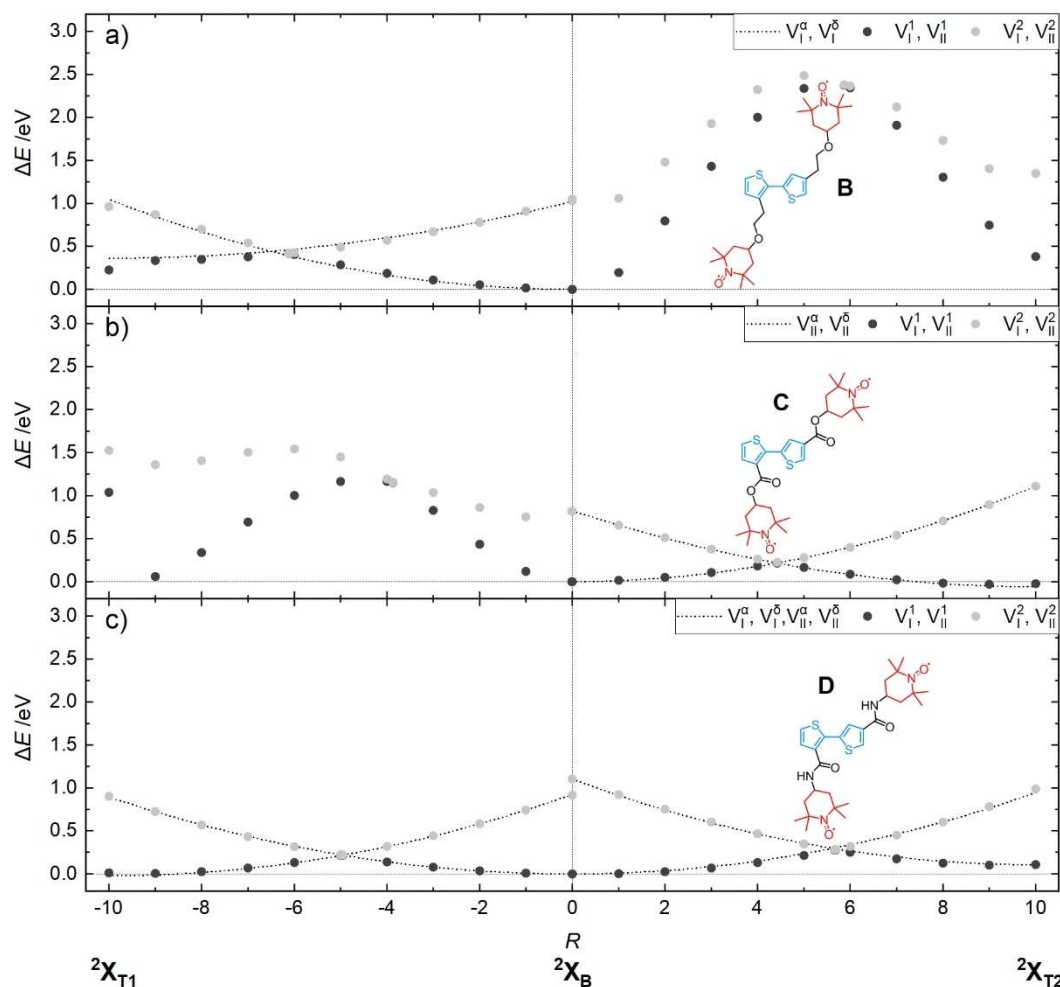| ORB model	$H_{\delta\alpha}^{dia}$ [eV] (FCD)	ΔG (discharging) [eV]	λ [eV]
$^2A_{T1} \rightleftarrows ^2A_B$	0.0075 (0.0020)	−0.363	1.674 0.821
$^2A_{T2} \rightleftarrows ^2A_B$	0.0048 (0.0012)	−0.128	1.540 0.821
$^2B_{T1} \rightleftarrows ^2B_B$	0.0004 (0.0001)	−0.225	0.961 0.828
$^2C_{T2} \rightleftarrows ^2C_B$	0.0060 (0.0016)	0.023	1.110 0.843
$^2D_{T1} \rightleftarrows ^2D_B$	0.0036 (0.0009)	−0.013	0.903 0.903
$^2D_{T2} \rightleftarrows ^2D_B$	0.0026 (0.0007)	−0.107	0.989 0.997
$^1E_T \rightleftarrows ^1E_B$	0.0018 (0.0009)	0.634	0.980 0.921
$^1F_T \rightleftarrows ^1F_B$	3.31E-05 (1.4E-05)	0.576	0.920 1.024

is merely 0.0048 eV. Hence, the coupling involving **T2** (inner TEMPO) is reduced to about two third in comparison the charge transfer involving **T1** (outer TEMPO). In addition, the electronic couplings were obtained using the fragment charge difference (FCD) method,[46,47] which yields with 0.0020 and 0.0012 eV ($^2A_{T1} \rightleftarrows ^2A_B$ and $^2A_{T2} \rightleftarrows ^2A_B$) values of similar magnitude, thus drawing a consistent picture.

Linker variation

The structural and chemical modification of the linker is expected to allow the tuning of the charge transfer processes in ORBs. Therefore, the influence of such systematic linker modification by variation of the CO-linker (**A**) using C_2O (**B**), COO (**C**), and CONH (**D**) was investigated in detail. In a similar fashion as described above, the ground state geometries of $^2X_{T1}$, ^2X_B, and $^2X_{T2}$ were fully equilibrated using the ωB97XD functional. Subsequently, the PESs connecting these species were evaluated at the CASSCF level of theory along LIICs (see Figure 3).

In case of **B** and **C**, harmonic PESs were only obtained along one of the two charge transfer coordinates, namely along $^2B_{T1} \rightleftarrows ^2B_B$ and $^2C_{T2} \rightleftarrows ^2C_B$. The non-harmonic PESs presumably originate from a rather complex underlying reaction coordinate. In these two cases, the reaction coordinate not only includes the planarization of the thiophene backbone but also a distinct rotation of the TEMPO around the linker. Therefore, the hole transfer process is very likely not sufficiently described by the LIIC, as interpolated coordinates force all structural alterations to occur simultaneously. An elaborate description of the reaction coordinate would involve more sophisticated structural changes during the charge transfer. A harmonic PES based on LIICs is only obtained if the reaction coordinate is mainly comprised of the planarization of the thiophene backbone.

ChemSusChem

Research Article
doi.org/10.1002/cssc.202201679

Chemistry
Europe
European Chemical
Societies Publishing

Figure 3. PESs of the hole transfer processes in **B**–**D** calculated by CASSCF. Dots represent energies of adiabatic states, corresponding potential energies V are labeled with Arabic numbers. Dotted lines represent respective diabatic surfaces, corresponding potential energies V are labeled with α for the acceptor state and δ for the donor state. Latin numbers denote the charge transfer reactions $^2X_{T1} \rightleftarrows {}^2X_B$ (I) or $^2X_{T2} \rightleftarrows {}^2X_B$ (II).

Analogous to **A**, the introduction of the C_2O-linker in **B** yields the triradical species as the thermodynamic equilibrium. Moreover, the magnitude of ΔG (−0.23 eV) and λ (0.96 and 0.83 eV) is in a similar range as for **A** (see Table 1). However, the electronic coupling of **B** (0.0004 eV) is decreased by one order of magnitude with respect to the reference system featuring the CO-linker. The small variance in driving forces and reorganization energies was to be expected, since both linkers (CO vs. C_2O) do not alter the electronic properties of the redox intermediates substantially. Likewise, the decreasing coupling is associated to the elongation of the linker and thus to the increased distance between the redox-active units. Similar behavior was already reported for charge transfer processes in iridium complexes.[48]

The introduction of the electron-withdrawing linkers [i.e., COO (**C**) and CONH (**D**)] leads to substantial changes in the driving forces. For **C**, ΔG gets positive (0.02 eV), thus the monoradicals $^2C_{T1}$ and $^2C_{T2}$ are slightly more stable than ^2C_B. Very likely, this change in driving force stems from the electron-withdrawing character of the ester. The −M effect destabilizes

any positive charge localized on the thiophene backbone, thereby destabilizing the ^MX_B species. In case of **D**, ΔG is negative as for **A** and **B**. For the reaction of $^2D_{T1} \rightleftarrows {}^2D_B$ its magnitude is almost zero (−0.01 eV), indicating an equilibrium which is only slightly shifted in favor of the triradical. However, the driving force of the hole transfer reaction along $^2D_{T2} \rightleftarrows {}^2D_B$, amounts to −0.11 eV. Hence, the triradical is distinctly more stable than the monoradical.

The electronic coupling of **C** along the $^2C_{T2} \rightleftarrows {}^2C_B$ coordinate is predicted with 0.0059 eV in a similar range as the electronic couplings of **A**. The electronic coupling for the charge transfer $^2D_{T1} \rightleftarrows {}^2D_B$ amounts to 0.0036 eV and for $^2D_{T2} \rightleftarrows {}^2D_B$ to 0.0026 eV. Compared to the two charge transfer processes in **A**, the electronic coupling is about halved. Furthermore, similar differences with respect to the TEMPO involved are predicted as shown previously for **A**.

Comparing the electronic couplings of all C_1-linkers, no trend regarding the chemical type of the linker is observed. If the chemical nature of the linker was of considerable impact on the electronic coupling, we would have expected the coupling

ChemSusChem

Research Article
doi.org/10.1002/cssc.202201679

**Chemistry
Europe**
European Chemical
Societies Publishing

of **C** and **D** to be more similar than the coupling of **C** or **D** and **A**. Yet, the couplings of **C** and **A** are much more alike than the couplings of **C** and **D**. Hence, it seems that the type of atom directly bonded to the TEMPO affects the coupling more than the electronic nature of the overall linker. Noteworthy, the size of the active space was kept constant for **A**–**D**, but the orbital composition of the active space changed for **D**. That means that the influence of linker orbitals increased and a mixing with the orbitals of the thiophene backbone was observed.

Strikingly, none of the molecules **A**–**D** exhibits identical driving forces for the reactions $^2X_{T1} \rightleftarrows {}^2X_B$ and $^2X_{T2} \rightleftarrows {}^2X_B$. Most likely, the reason lies within the broad range of different ground state geometries. The more versatile the linker is, the more local minima on the ground state PES are found and a broader distribution of driving forces results. This was exemplarily investigated by means of a conformer analysis of **A** as described in the computational details. Within this analysis, 509 conformers were determined within an energy range of 0.93 eV. This emphasizes the influence of structure-property relationships on the charge transfer processes and the resulting margin of charge transfer rates within one polymer (model). Such structure-property relationships are further revealed in **D**, in particular with respect to the driving forces. The ground state geometries of $^2D_{T1}$ and $^2D_{T2}$ are very similar with a root-mean-square deviation value of merely 0.41 Å. Yet, $^2D_{T2}$ is about 0.09 eV less stable than $^2D_{T1}$.

Ratio of redox-active units

Finally, the impact of the ratio of the redox-active units was assessed. Therefore, a terthiophene was decorated by one TEMPO moiety and connected by either a COO- (**E**) or a CONH- (**F**) linker. The PESs of **E** and **F** are shown in Figure 4. As the terthiophene-based ORB models feature only one TEMPO unit, only one hole transfer coordinate is defined. Both terthiophene model systems show a distinctive change in driving forces compared to their bithiophene variants (**C** and **D**). For the COO-linker, ΔG is increased from 0.02 eV to about 0.63 eV. In a similar fashion, ΔG was increased from −0.01 and −0.11 eV to 0.58 eV for the CONH-linker. Thus, the species ^1E_T and ^1F_T are further stabilized compared to ^2C_T and ^2D_T. This stabilization is rather counterintuitive, as the thiophene's ionization potential decreases with an increasing number of thiophene units.[49] Ionization potentials predicted by DFT are given in Figure S11 in the Supporting Information.

The reason for this stabilization likely originates from the applied computational protocol. Due to the computational demand, the relative size of the active space could not be adapted to the terthiophene system. For the bithiophene systems, five molecular orbitals per thiophene could be realized within the active space. In an analogous fashion, the respective terthiophene active space should comprise 20 electrons in 17 orbitals. Unfortunately, such a calculation was computationally not feasible at the CASSCF level of theory. Thus, we had to rely on the smaller active space (14,14) of the terthiophene.
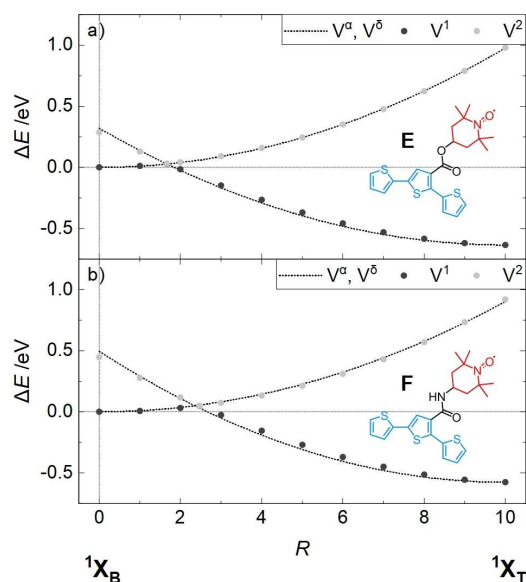
Figure 4. PESs of the hole transfer processes in (a) **E** and (b) **F** calculated by CASSCF. Dots represent energies of adiabatic states, corresponding potential energies V are labeled with Arabic numbers. Dotted lines represent respective diabatic surfaces, corresponding potential energies V are labeled with α for the acceptor state and δ for the donor state.

The electronic coupling of **E** is predicted to be 0.0018 eV. Hence, it is about a third of the value predicted for **C**. Likewise, a smaller coupling is observed for **F** in comparison to the respective bithiophene **D**. However, the coupling of **F** is, with about $3.3 \cdot 10^{-5}$ eV, two orders of magnitude smaller than for **D**.

Similar to the increase of ΔG, the decrease in coupling might be related to the proportionally smaller active space within the terthiophene systems. The smaller active space might also explain why the coupling of **F** is more affected than the coupling of **E**. As the active space of **F** illustrates a substantial mixing with the linker-based molecular orbitals, the ratio of orbitals of the thiophene backbone is further reduced.

Impact of dynamic correlation

Comparing the driving forces obtained using CASSCF with ionization potentials of TEMPO and a thiophene dimer, some major deficiencies unfold. The ionization potential of TEMPO lies at 6.9 eV[50], while the ionization potential of a thiophene dimer is found at 7.4 eV.[49] The experimental values hence suggest the monoradical species with the charge localized on the TEMPO to be more stable than the triradical with the charge localized on the thiophene dimer. Yet, CASSCF results indicate an opposite scenario. In contrast, DFT was able to predict the right direction of the driving force yet incapable to describe the dominant multiconfigurational character along the reaction coordinate. Thus, both static as well as dynamic correlation need to be addressed in order to assess the charge transfer phenomena in the present ORB model systems.

ChemSusChem

Research Article
doi.org/10.1002/cssc.202201679

**Chemistry
Europe**

European Chemical
Societies Publishing

In order to account for dynamic correlation, DLPNO-NEVPT2[51] was applied on the CASSCF reference wavefunction. Figure 5 depicts the PESs for **A** as obtained by CASSCF as well as based on DLPNO-NEVPT2. Surprisingly, only the TEMPO oxidation is stabilized substantially by approximately 1.3 eV, while the (diabatic) PES related to the thiophene oxidation as well as the harmonic shape of both PESs is hardly influenced upon application of second-order perturbation theory. However, as the driving forces of **A** (NEVPT2: 0.981 and 1.514 eV; CASSCF: −0.363 and −0.128 eV) are shifted to a greater extent than the magnitude of the reorganization energies (NEVPT2: 1.454 and 0.921 eV as well as 1.341 and 1.213 eV; CASSCF: 1.674 and 0.821 eV as well as 1.540 and 0.821 eV), the charge transfer between the redox-active sites is predicted within the inverted Marcus regime ($-\Delta G > \lambda$; see Table 2). Thus, the crossing of both diabatic states (δ and α) is not observed within the range of the interpolated structures connecting the respective equilibria. In contrast, the CASSCF results (accounting only for static correlation) indicate a direct Marcus scenario ($-\Delta G < \lambda$; see Table 1). Noteworthy, the electronic structure in the vicinity of

the crossing region between the diabatic states is dominated by static correlation. Therefore, we expect the influence of the NEVPT2 correction (and thus dynamic correlation) on the potential couplings to be of minor importance. Furthermore, the recalculation of potential couplings at the NEVPT2 level of theory would need extrapolated geometries due to the inverted Marcus regime. Yet, the extrapolation based on the linear-interpolated nature of the utilized reaction coordinate might lead to unphysically distorted structures. Therefore, we proceed with the couplings obtained by CASSCF. In consequence, merely driving forces and reorganization energies have been recalculated at the NEVPT2 level of theory for the remaining structures **B**–**F** within the equilibria of the respective redox intermediates.

Given by the NEVPT2-based driving forces, the impact of dynamic correlation on the bithiophene systems is striking. Driving forces for structures **A**–**D** are decreased by about 1.1 to 1.8 eV, while driving forces of **E** and **F** are less significantly affected. On the one hand, this effect likely stems from the different number of roots and therefore from the flexibility of
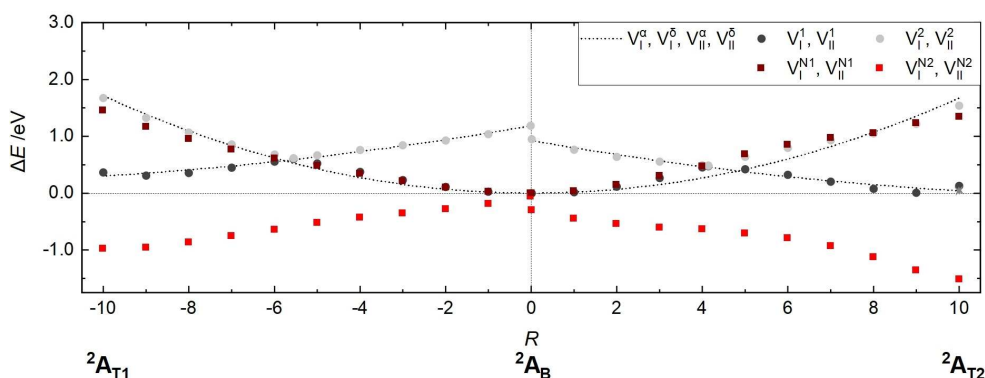
Figure 5. PESs of the hole transfer processes in **A** calculated by CASSCF (grey and black circles) and by DLNPO-NEVPT2 (dark red and red squares). Dots represent adiabatic energies; corresponding potential energies V are labeled with Arabic numbers. Dotted lines represent respective diabatic surfaces, corresponding potential energies V are labeled with α for the acceptor state and δ for the donor state. Latin numbers denote the charge transfer reactions $^{2}X_{T1} \rightleftarrows {}^{2}X_{B}$ (I) or $^{2}X_{T2} \rightleftarrows {}^{2}X_{B}$ (II).

Table 2. Electronic coupling $H_{\delta\alpha}^{dia}$, driving force ΔG (given for discharging, $^{M}X_{T} \rightarrow {}^{M}X_{B}$) and reorganization energy λ obtained at the DLPNO-NEVPT2 level of theory. Electronic couplings are calculated with the minimum energy splitting method (CASSCF energies); hole transfer rates are given based on semi-classical Marcus theory.

ORB model	$H_{\delta\alpha}^{dia}$ [eV]	ΔG (discharging) [eV]	λ [eV]	k_{ET}(Marcus) [s^{-1}] discharging	charging
$^{2}A_{T1} \rightleftarrows {}^{2}A_{B}$	0.0075	0.981	1.454	3.01E−06	1.76E+11
			0.921	1.65E−05	9.63E+11
$^{2}A_{T2} \rightleftarrows {}^{2}A_{B}$	0.0048	1.514	1.341	3.69E−15	2.70E+11
			1.213	2.32E−15	1.70E+11
$^{2}B_{T1} \rightleftarrows {}^{2}B_{B}$	0.0004	0.828	1.073	1.26E−05	1.76E+09
			0.702	2.16E−05	3.01E+09
$^{2}C_{T2} \rightleftarrows {}^{2}C_{B}$	0.0060	1.586	1.037	2.71E−17	3.37E+10
			0.878	1.88E−18	2.33E+09
$^{2}D_{T1} \rightleftarrows {}^{2}D_{B}$	0.0036	1.591	1.137	2.23E−17	3.42E+10
			0.844	2.31E−19	3.55E+08
$^{2}D_{T2} \rightleftarrows {}^{2}D_{B}$	0.0026	1.665	1.083	1.89E−19	5.20E+09
			1.013	6.87E−20	1.89E+09
$^{1}E_{T} \rightleftarrows {}^{1}E_{B}$	0.0018	0.502	1.025	9.98E+00	3.75E+09
			0.777	6.05E+01	2.27E+10
$^{1}F_{T} \rightleftarrows {}^{1}F_{B}$	3.31E−05	0.546	1.034	8.77E−04	1.90E+06
			0.829	3.66E−03	7.93E+06

ChemSusChem

Research Article
doi.org/10.1002/cssc.202201679

Chemistry Europe
European Chemical
Societies Publishing

the SA-CASSCF reference wavefunctions. In case of **A–D**, state-averaging was performed over four roots involving three degenerate triradical roots while in case of **E** and **F**, state-averaging was performed over three roots involving two degenerate diradical roots, see Figure S10 for details. Hence, the triradical state of **A–D** is stabilized to a greater extent than the diradical state of **E** and **F**. Yet, state-averaging exclusively over the two spin states directly involved in the hole transfer leads to a tremendous destabilization of the triradical species, while NEVPT2 on these wavefunctions tend to over-stabilize the triradical species again (Figure S9). Therefore, it is evident that all degenerate (spin) states should be considered in the state-averaging procedure as reflected by the experimental electro-chemical data (see below). On the other hand, the effect stems from the different relative sizes of the active spaces of the bi- (**A–D**) and terthiophene systems (**E** and **F**), which differ due to the computational demand as discussed previously. Hence, the influence of single and double excitations outside of the active space, originating from second-order perturbation theory on the SA-CASSCF reference wavefunction, varies.

In a similar fashion as discussed above for **A**, the reorganization energies obtained for **B–F** by means of SA-CASSCF vs. DLNPO-NEVPT2 do not differ substantially. However, and in contrast to CASSCF, NEVPT2 reveals a clear correlation of the linker's chemical nature and the predicted driving forces. Namely, the elongation of the C-chain within the linker from **A** to **B** only has a minor effect on the driving force. The driving force of the charge transfer $^2A_{T1} \rightarrow {}^2A_B$ is predicted to be 0.98 eV, the driving force for the charge transfer of $^2B_{T1} \rightarrow {}^2B_B$ is only 0.1 eV smaller. The electron-withdrawing linkers within **C** and **D** increase the driving force by about 0.6 to 0.7 eV. This was to be expected as the ionization potential of the thiophene dimer is further increased with the introduction of electron-withdrawing substituents. Thereby, the difference in ionization potentials of TEMPO and bithiophene is also further enhanced, and hence is the driving force of charge transfer. In contrast to the CASSCF results, the driving forces predicted by NEVPT2 for **C** (1.586 eV) and **D** (1.591 eV) are almost identical as both, ester- and amide-linker, exhibit an electron-withdrawing character.

Finally, the extension of the conjugated π-system from bithiophene to the terthiophene in **E** and **F** leads to a decrease in driving force by around 1 eV. This finding is consistent with the decrease in ionization potential by about 0.6 eV for the pure thiophene dimer to the thiophene trimer (Figure S11).

Therefore, both static and dynamic correlation need to be accounted for in order to reliably describe structure-property relationships in case of the present (poly)radical molecular systems.

Hole transfer rates

Based on the calculated thermodynamic properties (NEVPT2) and the potential couplings (CASSCF), rate constants for the underlying hole transfer processes were simulated for the present set of molecular ORB models. To this aim, semi-classical Marcus theory, which is widely applied to assess the kinetics of

charge transfer phenomena in nature and artificial applications, was adduced as a standard model to describe charge transfer processes.

Initially, the performance of semi-classical Marcus theory was benchmarked to numerical exact dissipative quantum dynamics (DQD) simulations that allow also superexchange phenomena and incomplete population transfer among the diabatic states of interest. To this aim, a detailed analysis of the CASSCF data was performed (see the Supporting Information for the full discussion). It was found that for small driving forces ($|\Delta G| \lesssim 0.1$ eV), Marcus theory is inadequate to describe the respective charge transfer process. This is mainly due to Marcus theory's incapability to describe incomplete charge transfer reactions. In such cases, DQDs predict the population of the donor or acceptor states to equilibrate somewhere between 1.00 and 0.00. In consequence, charge transfer rates predicted by Marcus theory are slower than the rates predicted by DQDs (divergence of 2 to 3 orders of magnitude). For the full discussion on the hole transfer kinetics at the CASSCF level of theory and the benchmark of Marcus theory vs. DQDs, the reader is referred to the Supporting Information. However, in case of DLNPO-NEVPT2, no driving force smaller than 0.50 eV was estimated. For such sizeable driving forces, both DQD and semi-classical Marcus theory predict a full population transfer and almost identical rate constants. Thus, within the given parameter regime based on the NEVPT2 data, Marcus theory yields a reliable description of the hole transfer kinetics.

The fastest charge transfer is observed for the charging reaction of the reference system in case of $^2A_B \rightarrow {}^2A_{T1}$ with a rate of 9.63×10^{11} s^{-1}. This translates to merely 1.1 ps for the charge transfer to proceed. On the one hand, this is due to the high coupling value. On the other hand, the driving force and reorganization energy are about the same magnitude. As the activation energy of the charge transfer is defined by Equation (1):

$$\Delta G^* = \frac{(\Delta G^{\circ} + \lambda)^2}{4\lambda} \tag{1}$$

The activation energy amounts to almost zero and allows an essentially barrierless population transfer between the donor and the acceptor state. Hence, it lies within the activationless Marcus region with $-\Delta G = \lambda$. It has to be noted that the influence of $-\Delta G \approx \lambda$ on the charge transfer efficiency is much higher than the size of the potential coupling, at least within the estimated range of couplings herein. The potential coupling of the charge transfer reaction $^2C_B \rightarrow {}^2C_{T2}$ is almost two times larger than the potential coupling for $^2D_B \rightarrow {}^2D_{T1}$. However, while the driving forces for each reaction is about 1.59 eV, the reorganization energies differ. In case of the $^2D_B \rightarrow {}^2D_{T1}$ reaction, the reorganization energy is 1.14 eV, which is about 0.1 eV smaller for $^2C_B \rightarrow {}^2C_{T2}$. Hence, the activation energy is smaller for the $^2D_B \rightarrow {}^2D_{T1}$ redox reaction, therefore compensating the smaller potential coupling. As a result, the hole transfer rate of $^2D_B \rightarrow {}^2D_{T1}$ amounts to 3.42×10^{10} s^{-1} (29.2 ps), while the respective rate of $^2C_B \rightarrow {}^2C_{T2}$ amounts to 3.37×10^{10} s^{-1} (29.7 ps),

rendering the latter slightly slower despite the higher coupling value.

The slowest charging rate is observed for $^1\mathbf{F_B} \rightarrow {}^1\mathbf{F_T}$ with merely $1.90 \times 10^6 \, s^{-1}$ (52.6 ms). This slow reaction stems from the very small electronic coupling ($3.3 \times 10^{-5} \, eV$). In case of $^1\mathbf{E_B} \rightarrow {}^1\mathbf{E_T}$, the transfer is approximately four orders of magnitude faster ($2.27 \times 10^{10} \, s^{-1}$) even though the driving force and the reorganization energies are very similar. Yet, the coupling value of $^1\mathbf{E_B} \rightarrow {}^1\mathbf{E_T}$ is about 50 times higher than the coupling value of $^1\mathbf{F_B} \rightarrow {}^1\mathbf{F_T}$ leading to a high divergence of the charge transfer rates.

Within the Marcus picture, the strong coupling with the bath, meaning the environment, for example, solvent or the polymer matrix, allows an efficient energy dissipation and therefore a complete charge transfer from the donor to the acceptor state. As stated above, such description is convenient for fast and strongly exergonic charge transfer reactions, yet endergonic reactions or equilibria are not accounted for. Hence, the discharging rates were calculated via the detailed balance condition based on the Marcus rates of the charging reaction ($k_{ET}^{B \rightarrow T}$) [Eq. (2)]:[41]

$$k_{ET}^{B \leftarrow T} = k_{ET}^{B \rightarrow T} e^{-\frac{\Delta G^{B \leftarrow T}}{k_B T}} \tag{2}$$

For all discharging reactions, the population transfer ($\mathbf{X_B} \leftarrow \mathbf{X_T}$) is thermodynamically unfavorable. As the focus of the current theoretical investigation is set exclusively on one cohesive half-cell without any applied current, this result is preferable. The chemical interpretation suggests that the charge is solely stored on the stable radical unit (i.e., the TEMPO) and is not delocalized onto the conductive backbone. This scenario reflects the initial aim of the design concept to provide efficient charge storage by means of the stable organic radical and conductivity via the aromatic polymer backbone. Hence, stable capacities of the half-cell should be accomplished.

Experimental studies

Based on the preceding theoretical studies, **C** and **F** were chosen to be synthesized. Due to a better synthetic accessibility, the structure of **C** was slightly modified, shifting the "outer" linkage position 4' to an inner one 3' (**C'**, see Figure 6). Both compounds were successfully synthesized using a two-step procedure based on literature-known reactions and commercially available starting compounds (for more details, see the Experimental Section).

Both compounds were subsequently characterized through cyclic voltammetry (Figure 6), revealing two redox processes. The first process is quite similar for both species: A chemically reversible redox reaction at a half-wave potential $E_{1/2}$ of 0.38 and 0.36 V vs. Fc^+/Fc was found for **C'** and **F**, respectively. This process is assigned to the reversible reaction of the TEMPO unit to the oxoammonium cation.[17] The second, irreversible process is assigned to the oxidation of the thiophene moiety of the respective species. Since the two systems possess different thiophene units, the observed electrochemical potentials are likewise different: The bithiophene-containing **C'** shows a rather high potential (peak potential E_p of 1.48 V vs. Fc^+/Fc at $100 \, mV\,s^{-1}$), while the terthiophene unit of **F**, which is known to be much easier oxidizable, leads to a lower potential ($E_p = 0.85$ V vs. Fc^+/Fc) of the second process. Consequently, also the energetic gaps between the two processes are rather different with 1.06 and 0.38 eV for **C'** and **F**, respectively.

As the TEMPO and the thiophene are oxidized separately and the initial oxidation of the TEMPO is favored, the differences of the electrochemical potentials might be compared qualitatively to the calculated driving forces. Still, it has to be kept in mind that the experimental values constitute the difference between the first and second oxidation process and not only the hole transfer within the once oxidized species. Furthermore, driving forces of **C** and **F** were calculated within the gaseous phase. Considering these points, driving forces of **C** and **F** match the difference in oxidation potential of **C'** and **F** rather well. With values of 1.59 eV for **C** and 0.54 eV for **F**, the driving forces are in the same order of magnitude as the differences in oxidation potential.
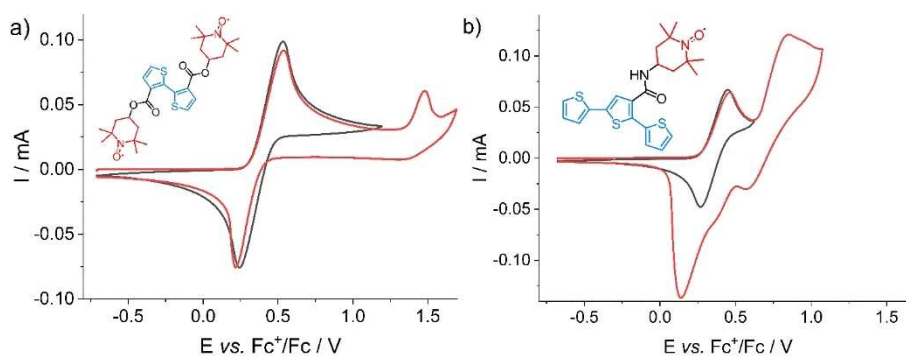
Figure 6. Cyclic voltammograms of the synthesized species (a) **C'** and (b) **F** involving either only the first (grey) or first and second (red) redox process (scan rate $100 \, mV\,s^{-1}$, CH_2Cl_2 with $0.1 \, M$ Bu_4NPF_6).

ChemSusChem

Research Article
doi.org/10.1002/cssc.202201679

Chemistry Europe
European Chemical
Societies Publishing

Conclusions

Within this contribution, a novel design approach for p-type electrode materials within organic radical batteries (ORBs) is proposed. Thereby, stable organic radicals [i.e., (2,2,6,6-tetramethylpiperidin-1-yl)oxyl (TEMPO)] are chemically linked to a thiophene-based conductive polymer backbone, thus aiming to overcome the shortcomings of conventional organic radical polymers and conjugated polymers suffering from low conductivity and unstable cell voltage, respectively. In consequence, the energy density of the electrode material is enhanced as addition of conductive agents is no longer required.

To thoroughly evaluate structure-property relationships in the frame of this new class of materials, we performed quantum chemical and quantum dynamical simulations to investigate the impact of the linker's length connecting the redox-active sites, its chemical nature (non-conjugated vs. conjugated), as well as the ratio of TEMPO vs. thiophene units based on six molecular model systems (**A**–**F**). Unfortunately, cost-efficient density functional theory (DFT) calculations proved to be insufficient to describe the electronic structure of these radical systems, due to the pronounced multiconfigurational character. In particular, quasi degenerate states in the vicinity of conical intersections are not correctly described. In order to allow a proper description of static correlation, we utilized the complete active space self-consistent field (CASSCF) methodology, while furthermore dynamic correlation was treated at the DLPNO-NEVPT2 level of theory.

This robust computational setup allows to thoroughly assess the charge transfer kinetics between the TEMPO and the conductive backbone, which translate in a macroscopic picture to the charging and discharging processes of the electrode material. Therefore, driving forces, reorganization energies and electronic couplings and, finally, rate constants for the respective charge transfer processes were calculated with respect to the substitution pattern. Our investigations reveal that the length of the linker has a tremendous impact on the potential coupling value, governing the hole transfer efficiency in the vicinity of the crossing between the two diabatic states of interest. Elongation of the alkyl linker by merely one methylene group (**A** to **B**) decreases the coupling by more than one order of magnitude. In contrast, the chemical nature of the linker has almost no influence on the coupling. Yet, replacing alkyl linkers with electron-deficient ester- or amide-moieties (**C** and **D**) affects the driving force for the underlying charge transfer to a great extent, favoring the oxidation of the TEMPO with respect to charge localization on the thiophene-based backbone by around 1 eV. Further, the oxidation potential of the (oligo)thiophene can be easily altered by modification of the ratio of TEMPO vs. thiophene units.

Finally, the (intramolecular) charge transfer kinetics among the redox-active units were evaluated. To this aim, semi-classical Marcus theory as well as DQD were utilized based on the previously obtained couplings as well as the thermodynamical properties (driving forces and reorganization energies) of the hole transfer processes. Due to the large driving forces, a complete charge transfer from the donor to the acceptor state is predicted. In fact, only hole transfer from the TEMPO towards the oligothiophene backbone is taking place spontaneously; back transfer from thiophene to TEMPO does not occur using detailed balance conditions. Hence, a stable charge localization on the TEMPO is possible within the potential p-type electrode materials, thus preventing a drop in capacity caused by spontaneous oxidation of the thiophene backbone. Finally, two of the initially computationally investigated structures, namely **C'** (a symmetric analogue of **C**) as well as **F**, were synthesized and electrochemically characterized. Both showed the expected reversible TEMPO-based redox reaction as well as a thiophene-related irreversible process. The latter is significantly shifted to higher potentials for **C'** compared to **F**, confirming the computational results.

As outlined in the introduction, a p-type electrode material should fulfill the following four criteria: (i) conductivity within the backbone, (ii) reasonably strong potential couplings, (iii) charge localization at the radical site for charge storage, and (iv) small activation energy to allow charge mobility. In the current contribution, we focused mainly on (ii)—(iv) as the conductivity of the backbone, (i), was already extensively studied for oligothiophenes.[20,52—54] In this context, the molecular model systems with C_1-linkers feature a reasonably high coupling, while for all molecular models, a charge localization on the TEMPO and a small activation energy was observed. However, increase of the thiophene backbone units per TEMPO decreases the driving force and hence destabilizes the charge localization. Therefore, the most promising molecular models are the ones with electron-withdrawing linkers and a higher driving force (i.e., **C**, **D**, **E**, and **F**).

Future joint synthetic-theoretical investigations will aim at extending these initial studies from molecular systems to the realm of materials. Therefore, and from the computational perspective, molecular dynamics within a multiscale approach will be performed to address fast charge transfer phenomena along the respective polymer strand (intramolecular) vs. potentially slow and weakly coupled charge transfer processes among different polymer strands. Experimentally, initial cell tests of the respective organic radical batteries are currently realized, pointing indeed to the desired electrochemical properties.

Experimental Section

Computational methods

All singly cationic molecular model systems comprising a thiophene-based backbone, decorated with chemically linked redox-active TEMPO radicals were optimized within Gaussian 16.[55] For each molecule (i.e., see **A**–**F** in Figure 1), the equilibrium structures of several redox species involved in the charging and discharging processes were obtained, i.e., within doublet multiplicity in case of **A**–**D** and within singlet multiplicity for **E** and **F**. These redox species localize the positive charge either on the nitroxide moiety of the TEMPO or on the thiophene backbone as shown exemplarily for **A** in Figure 1a. In case the charge is localized on the TEMPO for molecules **A**–**D**, a monoradical is formed, while for molecules **E** and **F**, a closed-shell species is obtained. However,

ChemSusChem

Research Article
doi.org/10.1002/cssc.202201679

**Chemistry
Europe**
European Chemical
Societies Publishing

if the (positive) charge is localized on the thiophene backbone, a triradical is yielded in case of **A–D**, whereas an opened-shell singlet is formed for **E** and **F** (diradical). In order to differentiate between the respective redox intermediates, the $^M X_C$ notation is used, where **M** labels the multiplicity of the species of the molecule **X** and **C** denotes the position of the charge, namely at the outer TEMPO (**T1**), the inner TEMPO (**T2**) or at the thiophene backbone (**B**).

DFT was applied using the range-separated functional ωB97XD.[42] Furthermore, Ahlrichs' def2tzvp[56] basis set was utilized for all DFT calculations. Vibrational mode analysis verified that all ground state geometries are (local) minima on their respective PESs.

Furthermore, a conformer search at the GFN2-xTB[57] level of theory was performed for **A**. For that purpose, the CREST[58] program was deployed. Subsequently, single point calculations were performed by means of the program ORCA 4.2.1[59,60] with the range-separated functional ωB97XD3[61] and the basis set def2-tzvp[56] for all obtained conformers.

The charge transfer from the TEMPO to the thiophene oligomer was investigated along effective intramolecular hole transfer coordinates. On that account, the respective species were linearly interpolated in internal coordinates (LIIC) using pysisyphus,[43] our lately introduced external optimizer that is aware of excited states. All equilibrium structures as well as interpolated geometries (LIICs) are available by means of the Zenodo open data repository under Ref. [62]. Subsequently, PESs were obtained by single point calculations along the LIIC. To this aim, TD-DFT was initially employed for **A** using the same density functional and basis set as for the preliminary ground state calculations. Furthermore, to allow a balanced description of the (poly)radical redox intermediates, multiconfigurational methods were applied. The state-averaged (SA)-CASSCF[44,45] approach as implemented in ORCA 4.2.1[59,60] was utilized. For **A–D**, an active space (15,13), comprising 15 electrons in 13 orbitals, was constructed. This includes six π_B and four π_B^* orbitals of the thiophene backbone as well as the SOMOs of the two nitroxide radicals (π_{NO}^*) and the π_{NO} orbital of the positively charged TEMPO moiety (see Figure 7 exemplarily for $^2 A_{T1}$ and Figures S12–S15 for details regarding **A–D**).

State averaging was performed over four roots, namely the doublet monoradical state of $^2 X_T$, the two triradical doublet states ($^2 X_B$), and the triradical quartet states ($^4 X_B$). The two roots of $^2 X_B$ are degenerate and only discriminated by their spin states (see Figure S10).

For **E** and **F**, active spaces of (14,14) were constructed (Figures S16 and S17). In case of **E**, six pairs of π_B/π_B^* orbitals were considered

for the thiophene backbone as well as the SOMO (π_{NO}^*) and the π_{NO} orbital of the nitroxide radical. The active space of **F** is set up in a similar fashion, except that the π_B-system features a slight mixing with amide-linker-based orbitals. The state averaging comprised the opened-shell singlet states (biradical), with one unpaired electron at the one TEMPO and the other in the HOMO of the thiophene backbone ($^1 X_B$), as well as the respective degenerate triplet state ($^3 X_B$) and the closed-shell singlet state with the positive charge at the TEMPO ($^1 X_T$).

For all (SA-)CASSCF calculations, the correlation consistent double zeta basis set cc-pVDZ[63] was employed. To speed up the calculations, the resolution of identity (RI) approximation[64] in combination with the "/c"-auxiliary basis set[65] was applied for integral transformations. The impact of dynamic correlation was evaluated for all LIICs between the redox intermediates of $^2 A_B$, $^2 A_{T1}$, and $^2 A_{T2}$ as well as for the redox intermediates $^2 B_B$, $^2 B_{T1}$, $^2 C_B$, $^2 C_{T2}$, $^2 D_B$, $^2 D_{T1}$, $^2 D_{T2}$, $^1 E_B$, $^1 E_T$, $^1 F_B$, and $^1 F_T$ at the DLPNO-NEVPT2[51] level of theory (i.e., applying second-order perturbation theory on the SA-CASSCF reference wavefunction). Truncation of the 4- and 3-pdm was set to 10^{-14} each. Accuracy of the DLPNO was set to 10^{-10}.

Finally, the kinetics of intramolecular hole transfer processes within **A–F** were assessed based on semi-classical Marcus theory.[66–68] In the Marcus picture, electron (or hole) transfer among the diabatic donor (δ) and acceptor (α) states is given by Equation (3):

$$k_{ET} = \frac{2\pi}{\hbar} \frac{\left| H_{\delta\alpha}^{dia} \right|^2}{\sqrt{4\pi\lambda k_B T}} e^{-\frac{(\Delta G+\lambda)^2}{4\lambda k_B T}} \tag{3}$$

Based on the obtained PESs (i.e., obtained at the CASSCF and NEVPT2 levels of theory), the potential coupling $H_{\delta\alpha}^{dia}$ (only CASSCF) between δ and α, the driving force ΔG and the reorganization energy λ were obtained. The potential couplings were calculated at the crossing of the two diabatic PESs as approximated by the point where the electronic configurations of δ and α feature an equal weight. At this point along the LIIC, the potential coupling was derived by means of Equation (4):

$$H_{\delta\alpha}^{dia} = \frac{1}{2}(E_2 - E_1) \tag{4}$$

where E_1 and E_2 are the potential energies of the two adiabatic states. In addition, the fragment charge difference (FCD) method[46,47] was applied at this geometry as implemented in Q-Chem 5.1.[69] Therefore, CAS-CI calculations were performed
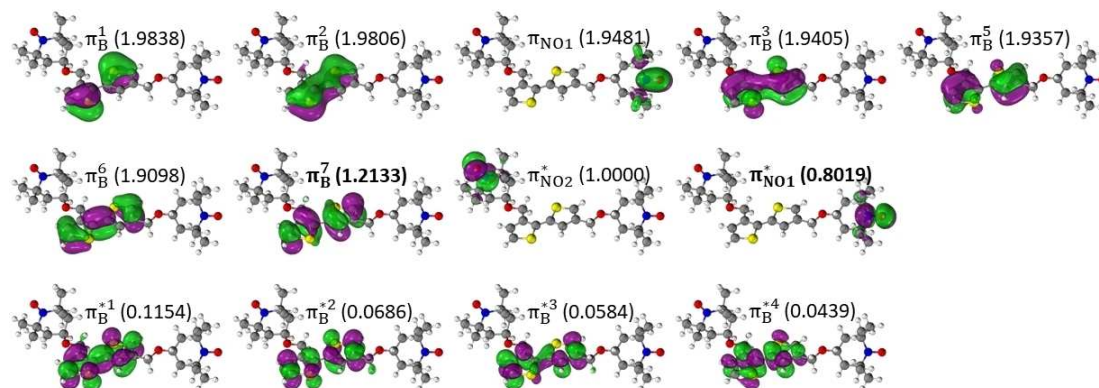
Figure 7. Composition of the active space (15,13) of $^2 A_{T1}$; average occupation numbers are given in parentheses. Frontier orbitals in the Hartree-Fock reference wavefunction as highlighted.

ChemSusChem

Research Article
doi.org/10.1002/cssc.202201679

**Chemistry
Europe**

European Chemical
Societies Publishing

exclusively for the roots of interest based on the converged SA-CASSCF wavefunctions. Thereby, the fragments were defined by the nitroxide radical(s) and the thiophene backbone. The resulting Mulliken charges as obtained for each fragment and for each root were used to calculate the FCD and in consequence $H_{\delta\alpha}^{dia}$.

The electronic nature of the diabatic states (δ and α) was traced by means of the CI vector of the respective CASSCF calculations along the LIIC. Driving forces and reorganization energies were obtained based on the energy levels of the states of interest within the previously optimized stationary points. Lately, this procedure was successfully applied and compared to quantum dynamical simulations in the scope of light-driven intramolecular and intermolecular electron transfer phenomena.[36,37]

Finally, dissipative quantum dynamics (DQD) were employed to validate the rates obtained by Marcus theory. Therefore, the recently introduced MACGIC-iQUAPI,[40,41] based on the iterative quasi-adiabatic propagator path integral (iQUAPI) approach, was applied. In contrast to the widely applied Marcus theory, MACGIC-iQUAPI is able to successfully cover parameter regimes of coherent and incoherent energy and charge transfer processes in dissipative quantum systems subject to a classical environment with long-time bath memory. For the DQD simulations, the temperature was set to 295 K, while an ohmic spectral density (width of 2000 cm^{-1}) and a maximum integration frequency of 32000 cm^{-1} were used. The filter threshold was adjusted to 1×10^{-8} and an effective mask size of 48 was utilized. Systematically, all systems were propagated using a maximum memory time of 800 time steps, while the length of the time steps were determined for each simulation individually. The population transfer from the donor state to the acceptor state is assumed to be a first-order reaction. Therefore, the rate constant of the hole transfer was determined by fitting the population of the donor state (N_δ) to the exponential function [Eq. (5)]:

$$f(x) = (1 - N_\delta)e^{-k_{DQD}(t-t_0)} + N_\delta \qquad (5)$$

In case of non-converging MACGIC-iQUAPI simulations, the detailed balance condition was applied by an in-house written python script. Thereby, the rate constant is calculated via Marcus theory while the population of the donor and acceptor state is calculated via the Boltzmann distribution [see Eq. (2)]. Again, the population transfer is assumed to be a first-order reaction. Further, the population of the donor state is also fitted to [Eq. (5)].

Materials

All materials were obtained from commercial sources. Solvents were distilled prior to use. Thin-layer chromatography (TLC) was performed on pre-coated TLC sheets Alugram® Sil/G UV254, 0.20 mm silica gel 60, purchased from Macherey-Nagel.

Column chromatography was performed on a Combiflash Rf 200 on silica RediSep-Rf cartridges (35–60 μm, 100 Å pore-size). ^{1}H spectra were measured on a Bruker AC 300 spectrometer at 298 K. Chemical shifts are reported in parts per million (ppm, δ scale) relative to the residual signal of the deuterated solvent. Electrospray ionization (ESI) mass spectrometry measurements were performed on a micrOTOF Q-II ESI time-of-flight (ESI-TOF) mass spectrometry system (Bruker Daltonics Inc.). Elemental analyses were carried out using a CHN(s) analyzer Euro EA300 (HEKATech GmbH, Germany).
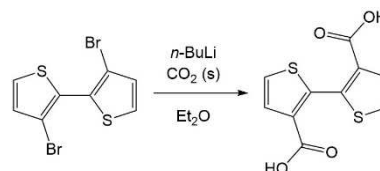
Cyclic voltammetry experiments were performed using a Biologic VMP 300 potentiostat at room temperature under argon atmosphere. Solutions consisted of 3 mL CH_2Cl_2 with 0.1 M Bu_4NPF_6 and 5 mg of the studied compound. A three-electrode setup with a glassy-carbon working electrode (3 mm diameter), a platinum wire counter electrode and a $AgNO_3$/Ag/CH_3CN reference electrode was used. After the measurements, ferrocene was added and measured in order to have a reliable potential reference. Half-wave potentials are calculated as average value of oxidation and reduction peak potentials. Energetic differences are determined from the onset potentials of the redox waves.
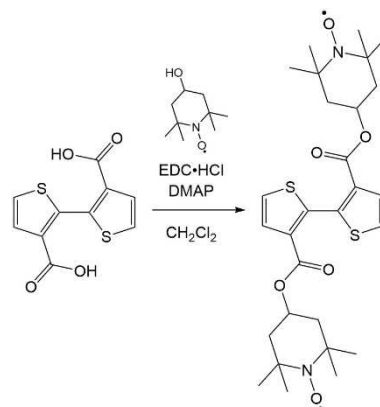
Synthesis of bis(2,2,6,6-tetramethylpiperidinyl-N-oxyl-4-yl)-[2,2′-bithiophene]-3,3′-dicarboxylate (C′)

2,2′-Bithiophene-3,3′-dicarboxylic acid: The synthesis was carried out according to literature procedure (Scheme 1).[70] 260 mg (1.02 mmol, 55%) of an off-white solid was obtained. ^{1}H NMR (300 MHz, DMSO-d_6): $\delta = 7.41$–7.66 (dd, 4H), 12.8 ppm (s, 2H).

Bis(2,2,6,6-tetramethylpiperidinyl-*N*-oxyl-4-yl)-[2,2′-bithiophene]-3,3′-dicarboxylate (C′): The synthesis was derived from a literature procedure (Scheme 2).[71] In a 25 mL round-bottom flask, 4-hydroxy-2,2,6,6-tetramethyl-piperidinyl-*N*-oxyl (680 mg, 3.95 mmol) and 4-(dimethylamino)pyridine (26 mg, 0.21 mmol) were dissolved in 10 mL of dry dichloromethane. The solution was cooled to 0 °C and 2,2′-bithiophene-3,3′-dicarboxylic acid (250 mg, 0.98 mmol) was added; the turbid mixture was stirred for 15 min. Subsequently, 1-ethyl-3-(3-dimethylaminopropyl)carbodiimide hydrochloride (420 mg, 2.20 mmol) in 10 mL of dichloromethane was added, and the mixture was allowed to heat to room temperature resulting in a clear, red solution. The solution was then stirred at room temperature for 4 days. The mixture was afterwards washed with water (4×20 mL) and brine (20 mL) and dried over Mg_2SO_4. The Mg_2SO_4 was filtered off and the solvent was removed under vacuum. The resulting solid was purified via column chromatography (40 g silica cartridge; eluent gradient: hexane/ethyl acetate 1:0 → 3:1; product at 12–16 column volumes, $R_f = 0.07$) to yield 250 mg of a pale-red solid (0.44 mmol, 45%). m/z (ESI/MS): 562, 563, 564, 565 (M^+), 585, 586, 587, 588 ($M + Na^+$), 601, 602, 603, 604, 605 ($M + K^+$), 1147,

Scheme 1. Synthesis of 2,2′-bithiophene-3,3′-dicarboxylic acid.
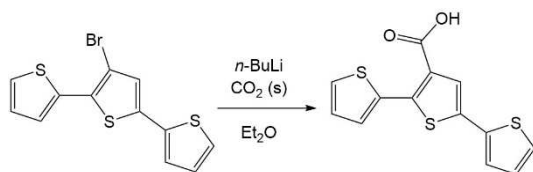

Scheme 2. Synthesis of **C′**.

ChemSusChem

Research Article
doi.org/10.1002/cssc.202201679

**Chemistry
Europe**
European Chemical
Societies Publishing

1148, 1149, 1150, 1151, 1152 (2 M+Na⁺), 1163, 1164, 1165, 1166, 1167 (2 M+K⁺). HR-MS ([C$_{28}$H$_{38}$N$_2$O$_6$S$_2$]⁺): calculated: 562.2166, found: 562.2149, error: 3.0 ppm. Elemental analysis calculated for C$_{28}$H$_{38}$N$_2$O$_6$S$_2$: C 59.76, H 6.81, N 4.98, S 11.39. Found C 59.45, H 6.82, N 5.14, S 11.33.

Synthesis of (2,2,6,6-tetramethylpiperidinyl-N-oxyl-4-yl)-[2,2′:5′,2″-terthiophene]-3′-carboxamide (F)

2,2′:5′,2″-Terthiophene-3′-carboxylic acid: The synthesis was derived from a literature procedure (Scheme 3).[70] A solution of *n*-butyllithium (1.6 M in hexanes, 1.6 mL, 2.6 mmol) was added under argon at −70 °C to 22 mL of dry diethyl ether. The solution was stirred for 20 min. 3′-Bromo-2,2′:5′,2″-terthiophene (600 mg, 1.83 mmol) was dissolved under argon in 8 mL of dry diethyl ether. The solution was added dropwise to the *n*-butyllithium solution over 1 h maintaining a temperature of approximately −70 °C. The resulting mixture was stirred for 1 h at −70 °C. Subsequently, 1 g of solid carbon dioxide was added under argon and the mixture was stirred for another 1 h, resulting in a pale-orange, turbid mixture. 50 μL of methanol was added for quenching and the mixture was allowed to heat up to room temperature. The formed precipitate was filtered off and washed with ice-cold diethyl ether; the resulting solid was dried under vacuum. The solid was then dissolved in 8 mL of water. 1 M hydrochloric acid was added to reach pH 1, resulting in the formation of a yellow precipitate, which was filtered off and washed with 0.1 M hydrochloric acid. The obtained solid was dried under vacuum resulting in 300 mg (1.03 mmol, 55%) of a yellow solid. ^{1}H NMR (300 MHz, DMSO-d_6): δ = 7.13 (ddd, 2H, J = 4.91, 3.77, 0.91 Hz), 7.42 (dd, 1H, J = 3.65, 1.14 Hz), 7.52 (s, 1H), 7.54 (dd, 1H, J = 3.65, 1.14 Hz), 7.59 (dd, 1H, J = 5.03, 1.14 Hz), 7.69 ppm (dd, 1H, J = 5.14, 1.26 Hz). ^{13}C NMR (75 MHz, DMSO-d_6): δ = 125.53 (s), 126.83 (s), 126.87 (s), 128.02 (s), 129.03 (s), 129.18 (s), 129.66 (s), 130.54 (s), 133.60 (s), 134.62 (s), 135.33 (s), 139.48 (s), 164.40 ppm (s). *m/z* (ESI/MS): 315, 316, 317, 318 (M+Na⁺), 331, 332, 333, 334 (M+K⁺), 607, 608, 609, 610, 611 (2 M+Na⁺), 623, 624, 625, 626, 627 (2 M+K⁺). HR-MS ([C$_{13}$H$_8$O$_2$S$_3$+Na]⁺): calculated: 314.9579, found: 314.9586, error: 2.4 ppm.

(2,2,6,6-Tetramethylpiperidinyl-*N*-oxyl-4-yl)-[2,2′:5′,2″-terthiophene]-3′-carboxamide (F): The synthesis was derived from a literature procedure (Scheme 4).[71] In a 10 mL round-bottom flask, 4-amino-2,2,6,6-tetramethyl-piperidinyl-*N*-oxyl (280 mg, 1.63 mmol) and 4-(dimethylamino)pyridine (14 mg, 0.11 mmol) were dissolved in 10 mL of dry dichloromethane. The solution was cooled to 0 °C and 2,2′:5′,2″-terthiophene-3′-carboxylic acid (260 mg, 0.88 mmol) was added; the turbid mixture was stirred for 15 min. Subsequently, 1-ethyl-3-(3-dimethylaminopropyl)carbodiimide hydrochloride (180 mg, 0.93 mmol) was added and the mixture was allowed to heat to room temperature resulting in a clear, red solution. The solution was then stirred at room temperature for 3 days. The mixture was afterwards washed with water (4×10 mL) and brine (10 mL) and dried over Mg$_2$SO$_4$. The Mg$_2$SO$_4$ was filtered off and the solvent was removed under vacuum. The resulting solid was purified via column chromatography (40 g silica cartridge; eluent gradient: hexane/ethyl acetate 1:0 → 2:1; product at 6–7 column volumes, R_f = 0.15) to yield 235 mg of a pale-red solid (0.53 mmol, 60%). *m/z* (ESI/MS): 445, 446, 447, 448 (M⁺), 468, 469, 470, 471 (M+Na⁺), 484, 485, 486, 487, 488 (M+K⁺). HR-MS ([C$_{22}$H$_{25}$N$_2$O$_2$S$_3$]⁺): calculated: 445.1073, found: 445.1067, error: 1.2 ppm. Elemental analysis calculated for C$_{22}$H$_{25}$N$_2$O$_2$S$_3$: C 59.30, H 5.65, N 6.29, S 21.58. Found C 59.38, H 5.74, N 6.35, S 21.88.

Conflict of Interest

The authors declare no conflict of interest.

Data Availability Statement

The data that support the findings of this study are openly available in Zenodo at https://doi.org/10.5281/zenodo.6997917, reference number 62.

Keywords: charge transfer · computational chemistry · energy storage · organic radical batteries · TDDFT

Scheme 3. Synthesis of 2,2′:5′,2″-terthiophene-3′-carboxylic acid.

Scheme 4. Synthesis of **F**.

[1] J. B. Goodenough, Y. Kim, *Chem. Mater.* **2010**, *22*, 587–18013.
[2] J. M. Tarascon, M. Armand, *Nature* **2001**, *414*, 359–367.
[3] C. Vaalma, D. Buchholz, M. Weil, S. Passerini, *Nat. Rev. Mater.* **2018**, *3*, 652.
[4] W. Lv, Z. Wang, H. Cao, Y. Sun, Y. Zhang, Z. Sun, *ACS Sustainable Chem. Eng.* **2018**, *6*, 1504–1521.
[5] T. Georgi-Maschler, B. Friedrich, R. Weyhe, H. Heegn, M. Rutz, *J. Power Sources* **2012**, *207*, 173–182.
[6] D. Larcher, J.-M. Tarascon, *Nat. Chem.* **2015**, *7*, 19–29.
[7] P. Poizot, F. Dolhem, *Energy Environ. Sci.* **2011**, *4*, 2003–2019.
[8] A. Gandini, T. M. Lacerda, A. J. F. Carvalho, E. Trovatti, *Chem. Rev.* **2016**, *116*, 1637–1669.
[9] K.-H. Choi, D. B. Ahn, S.-Y. Lee, *ACS Energy Lett.* **2018**, *3*, 220–236.
[10] C. K. Chiang, *Polymer* **1981**, *22*, 1454–1456.

[11] D. MacInnes, M. A. Druy, P. J. Nigrey, D. P. Nairns, A. G. MacDiarmid, A. J. Heeger, *J. Chem. Soc. Chem. Commun.* **1981**, 317–319.

[12] J. F. Mike, J. L. Lutkenhaus, *J. Polym. Sci. Part B* **2013**, *51*, 468–480.

[13] P. Bäuerle, *Adv. Mater. (Weinheim, Ger.)* **1993**, *5*, 879–886.

[14] P. Novák, K. Müller, K. S. V. Santhanam, O. Haas, *Chem. Rev.* **1997**, *97*, 207–282.

[15] A. F. Diaz, K. K. Kanazawa, G. P. Gardini, *J. Chem. Soc. Chem. Commun.* **1979**, 635–636.

[16] A. F. Diaz, J. I. Castillo, J. A. Logan, W.-Y. Lee, *J. Electroanal. Chem. Interfacial Electrochem.* **1981**, *129*, 115–132.

[17] C. Friebe, U. S. Schubert, *Top. Curr. Chem.* **2017**, *375*, 19.

[18] F. Li, D. N. Gore, S. Wang, J. L. Lutkenhaus, *Angew. Chem.* **2017**, *129*, 9988–9991; *Angew. Chem. Int. Ed.* **2017**, *56*, 9856–9859.

[19] J. Bartuš, *J. Macromol. Sci. Chem.* **1991**, *28*, 917–924.

[20] T. P. Kaloni, P. K. Giesbrecht, G. Schreckenbach, M. S. Freund, *Chem. Mater.* **2017**, *29*, 10248–10283.

[21] K. Nakahara, S. Iwasa, M. Satoh, Y. Morioka, J. Iriyama, M. Suguro, E. Hasegawa, *Chem. Phys. Lett.* **2002**, *359*, 351–354.

[22] K. Koshika, N. Chikushi, N. Sano, K. Oyaizu, H. Nishide, *Green Chem.* **2010**, *12*, 1573.

[23] Y. Luo, F. Zheng, L. Liu, K. Lei, X. Hou, G. Xu, H. Meng, J. Shi, F. Li, *ChemSusChem* **2020**, *13*, 2239–2244.

[24] K. Hatakeyama-Sato, H. Wakamatsu, R. Katagiri, K. Oyaizu, H. Nishide, *Adv. Mater. (Weinheim, Ger.)* **2018**, *30*, e1800900.

[25] J. Blumberger, *Phys. Chem. Chem. Phys.* **2008**, *10*, 5651–5667.

[26] L. Hu, M. Farrokhnia, J. Heimdal, S. Shleev, L. Rulíšek, U. Ryde, *J. Phys. Chem. B* **2011**, *115*, 13111–13126.

[27] C. A. Hurd, N. A. Besley, D. Robinson, *J. Comput. Chem.* **2017**, *38*, 1431–1437.

[28] T. Kubar, M. Elstner, *J. Phys. Chem. B* **2008**, *112*, 8788–8798.

[29] L. W. Ungar, N. F. Scherer, G. A. Voth, *Biophys. J.* **1997**, *72*, 5–17.

[30] J. P. Menzel, V. Boeije, T. M. A. Bakker, J. Belić, J. N. H. Reek, H. J. M. de Groot, L. Visscher, F. Buda, *ChemSusChem* **2022**, *15*, e202200594.

[31] A. R. Menzeleev, N. Ananth, T. F. Miller, *J. Chem. Phys.* **2011**, *135*, 74106.

[32] H. Oberhofer, J. Blumberger, *J. Chem. Phys.* **2009**, *131*, 64101.

[33] Y. Shao, H. J. M. de Groot, F. Buda, *ChemSusChem* **2021**, *14*, 3155–3162.

[34] M.-L. Tan, E. A. Dolan, T. Ichiye, *J. Phys. Chem. B* **2004**, *108*, 20435–20441.

[35] S. Záliš, J. Heyda, F. Šebesta, J. R. Winkler, H. B. Gray, A. Vlček, *Proc. Natl. Acad. Sci. USA* **2021**, *118*.

[36] A. Koch, D. Kinzel, F. Dröge, S. Gräfe, S. Kupfer, *J. Phys. Chem. C* **2017**, *121*, 16066–16078.

[37] S. Kupfer, D. Kinzel, M. Siegmann, J. Philipp, B. Dietzek, S. Gräfe, *J. Phys. Chem. C* **2018**, *122*, 3273–3285.

[38] M. Staniszewska, S. Kupfer, J. Guthmuller, *Chem. Eur. J.* **2018**, *24*, 11166–11176.

[39] M. Staniszewska, S. Kupfer, J. Guthmuller, *J. Phys. Chem. C* **2019**, *123*, 16003–16013.

[40] M. Richter, B. P. Fingerhut, *J. Chem. Phys.* **2017**, *146*, 214101.

[41] M. Richter, B. P. Fingerhut, *Faraday Discuss.* **2019**, *216*, 72–93.

[42] J.-D. Chai, M. Head-Gordon, *Phys. Chem. Chem. Phys.* **2008**, *10*, 6615–6620.

[43] J. Steinmetzer, S. Kupfer, S. Gräfe, *Int. J. Quantum Chem.* **2021**, *121*, 11856.

[44] H.-J. Werner, W. Meyer, *J. Chem. Phys.* **1980**, *73*, 2342–2356.

[45] H.-J. Werner, W. Meyer, *J. Chem. Phys.* **1981**, *74*, 5794–5801.

[46] A. A. Voityuk, *Phys. Chem. Chem. Phys.* **2012**, *14*, 13789–13793.

[47] A. A. Voityuk, N. Rösch, *J. Chem. Phys.* **2002**, *117*, 5607–5616.

[48] M. Baldoni, A. Lorenzoni, A. Pecchia, F. Mercuri, *Phys. Chem. Chem. Phys.* **2018**, *20*, 28393–28399.

[49] D. Jones, M. Guerra, L. Favaretto, A. Modelli, M. Fabrizio, G. Distefano, *J. Phys. Chem.* **1990**, *94*, 5761–5766.

[50] D. Kubala, K. Regeta, R. Janečková, J. Fedor, S. Grimme, A. Hansen, P. Nesvadba, M. Allan, *Mol. Phys.* **2013**, *111*, 2033–2040.

[51] Y. Guo, K. Sivalingam, E. F. Valeev, F. Neese, *J. Chem. Phys.* **2016**, *144*, 94111.

[52] P. Bai, E. Li, E. A. Ong, P. Collier, K. P. Loh, *Phys. Status Solidi A* **2007**, *204*, 1876–1881.

[53] B. Beach, D. Sauriol, P. Derosa, *J. Electron. Mater.* **2016**, *45*, 2150–2159.

[54] S. M. Bouzzine, G. Salgado-Morán, M. Hamidi, M. Bouachrine, A. G. Pacheco, D. Glossman-Mitnik, *J. Chem.* **2015**, *2015*, 296386, https://www.hindawi.com/journals/jchem/2015/296386/.

[55] M. J. Frisch, G. W. Trucks, H. B. Schlegel, G. E. Scuseria, M. A. Robb, J. R. Cheeseman, G. Scalmani, V. Barone, G. A. Petersson, H. Nakatsuji, X. Li, M. Caricato, A. V. Marenich, J. Bloino, B. G. Janesko, R. Gomperts, B. Mennucci, H. P. Hratchian, J. V. Ortiz, A. F. Izmaylov, J. L. Sonnenberg, D. Williams-Young, F. Ding, F. Lipparini, F. Egidi, J. Goings, B. Peng, A. Petrone, T. Henderson, D. Ranasinghe, V. G. Zakrzewski, J. Gao, N. Rega, G. Zheng, W. Liang, M. Hada, M. Ehara, K. Toyota, R. Fukuda, J. Hasegawa, M. Ishida, T. Nakajima, Y. Honda, O. Kitao, H. Nakai, T. Vreven, K. Throssell, J. A. Montgomery, Jr., J. E. Peralta, F. Ogliaro, M. J. Bearpark, J. J. Heyd, E. N. Brothers, K. N. Kudin, V. N. Staroverov, T. A. Keith, R. Kobayashi, J. Normand, K. Raghavachari, A. P. Rendell, J. C. Burant, S. S. Iyengar, J. Tomasi, M. Cossi, J. M. Millam, M. Klene, C. Adamo, R. Cammi, J. W. Ochterski, R. L. Martin, K. Morokuma, O. Farkas, J. B. Foresman, D. J. Fox, Gaussian 16, Gaussian, Inc., Wallingford CT, **2016**.

[56] F. Weigend, R. Ahlrichs, *Phys. Chem. Chem. Phys.* **2005**, *7*, 3297–3305.

[57] C. Bannwarth, S. Ehlert, S. Grimme, *J. Chem. Theory Comput.* **2019**, *15*, 1652–1671.

[58] P. Pracht, F. Bohle, S. Grimme, *Phys. Chem. Chem. Phys.* **2020**, *22*, 7169–7192.

[59] F. Neese, *Wiley Interdiscip. Rev.: Comput. Mol. Sci.* **2012**, *2*, 73–78.

[60] F. Neese, *Wiley Interdiscip. Rev.: Comput. Mol. Sci.* **2018**, *8*, 33.

[61] Y.-S. Lin, G.-D. Li, S.-P. Mao, J.-D. Chai, *J. Chem. Theory Comput.* **2013**, *9*, 263–272.

[62] C. Zens, **2022**, "Trajectories used for Tailoring Charge Transfer Kinetics in Organic Radical Batteries", https://zenodo.org/, DOI: 10.5281/zenodo.6997917.

[63] T. H. Dunning, *J. Chem. Phys.* **1989**, *90*, 1007–1023.

[64] F. Weigend, M. Kattannek, R. Ahlrichs, *J. Chem. Phys.* **2009**, *130*, 164106.

[65] F. Weigend, A. Köhn, C. Hättig, *J. Chem. Phys.* **2002**, *116*, 3175–3183.

[66] R. A. Marcus, *J. Chem. Phys.* **1956**, *24*, 966–978.

[67] R. A. Marcus, *J. Chem. Phys.* **1965**, *43*, 679–701.

[68] R. A. Marcus, *Angew. Chem. Int. Ed. Engl.* **1993**, *32*, 1111–1121.

[69] Y. Shao, Z. Gan, E. Epifanovsky, A. T. B. Gilbert, M. Wormit, J. Kussmann, A. W. Lange, A. Behn, J. Deng, X. Feng, D. Ghosh, M. Goldey, P. R. Horn, L. D. Jacobson, I. Kaliman, R. Z. Khaliullin, T. Kuś, A. Landau, J. Liu, E. I. Proynov, Y. M. Rhee, R. M. Richard, M. A. Rohrdanz, R. P. Steele, E. J. Sundstrom, H. L. Woodcock, P. M. Zimmerman, D. Zuev, B. Albrecht, E. Alguire, B. Austin, G. J. O. Beran, Y. A. Bernard, E. Berquist, K. Brandhorst, K. B. Bravaya, S. T. Brown, D. Casanova, C.-M. Chang, Y. Chen, S. H. Chien, K. D. Closser, D. L. Crittenden, M. Diedenhofen, R. A. DiStasio, H. Do, A. D. Dutoi, R. G. Edgar, S. Fatehi, L. Fusti-Molnar, A. Ghysels, A. Golubeva-Zadorozhnaya, J. Gomes, M. W. D. Hanson-Heine, P. H. P. Harbach, A. W. Hauser, E. G. Hohenstein, Z. C. Holden, T.-C. Jagau, H. Ji, B. Kaduk, K. Khistyaev, J. Kim, J. Kim, R. A. King, P. Klunzinger, D. Kosenkov, T. Kowalczyk, C. M. Krauter, K. U. Lao, A. D. Laurent, K. V. Lawler, S. V. Levchenko, C. Y. Lin, F. Liu, E. Livshits, R. C. Lochan, A. Luenser, P. Manohar, S. F. Manzer, S.-P. Mao, N. Mardirossian, A. V. Marenich, S. A. Maurer, N. J. Mayhall, E. Neuscamman, C. M. Oana, R. Olivares-Amaya, D. P. O'Neill, J. A. Parkhill, T. M. Perrine, R. Peverati, A. Prociuk, D. R. Rehn, E. Rosta, N. J. Russ, S. M. Sharada, S. Sharma, D. W. Small, A. Sodt, T. Stein, D. Stück, Y.-C. Su, A. J. W. Thom, T. Tsuchimochi, V. Vanovschi, L. Vogt, O. Vydrov, T. Wang, M. A. Watson, J. Wenzel, A. White, C. F. Williams, J. Yang, S. Yeganeh, S. R. Yost, Z.-Q. You, I. Y. Zhang, X. Zhang, Y. Zhao, B. R. Brooks, G. K. L. Chan, D. M. Chipman, C. J. Cramer, W. A. Goddard, M. S. Gordon, W. J. Hehre, A. Klamt, H. F. Schaefer, M. W. Schmidt, C. D. Sherrill, D. G. Truhlar, A. Warshel, X. Xu, A. Aspuru-Guzik, R. Baer, A. T. Bell, N. A. Besley, J.-D. Chai, A. Dreuw, B. D. Dunietz, T. R. Furlani, S. R. Gwaltney, C.-P. Hsu, Y. Jung, J. Kong, D. S. Lambrecht, W. Liang, C. Ochsenfeld, V. A. Rassolov, L. V. Slipchenko, J. E. Subotnik, T. van Voorhis, J. M. Herbert, A. I. Krylov, P. M. W. Gill, M. Head-Gordon, *Mol. Phys.* **2015**, *113*, 184–215.

[70] J. A. Letizia, M. R. Salata, C. M. Tribout, A. Facchetti, M. A. Ratner, T. J. Marks, *J. Am. Chem. Soc.* **2008**, *130*, 9679–9694.

[71] M. Aydın, B. Esat, Ç. Kılıç, M. E. Köse, A. Ata, F. Yılmaz, *Eur. Polym. J.* **2011**, *47*, 2283–2294.